Nanoscale Horizons

ROYAL SOCIETY OF CHEMISTRY

COMMUNICATION

View Article Online
View Journal | View Issue

Cite this: *Nanoscale Horiz.*, 2025, **10**, 1660

Received 13th April 2025,
Accepted 3rd June 2025

DOI: 10.1039/d5nh00237k

rsc.li/nanoscale-horizons

G-quadruplex-driven molecular disassembly and type I-to-type II photophysical conversion of a heavy-atom-free photosensitizer for site-specific oxidative damage†

Karolina Saczuk,[a] Maria V. Cottini,[b] Marta Dudek,[a] Leszek M. Mazur,[a] Dario Puchán Sánchez,[c] Lucía López-Pacios,[d] Ahmad Kassem,[c] Katarzyna Matczyszyn,[a] Juan J. Nogueira,[de] Cyrille Monnereau,[f] Lara Martínez-Fernández,*[g] Jan Jamroskovic,[b] Clément Cabanetos*[c] and Marco Deiana*[a]

G-quadruplex (G4)-targeted photosensitizers (PSs) are advancing precision oncology by confining DNA damage to malignant cells while sparing healthy tissue. Yet, molecular-level studies on the mechanisms and dynamics of G4 structure damage under PSs light-activation are limited. Here, we introduce DBI-POE, an activatable, heavy-atom-free PS derived from the G4-specific sulfur-substituted dibenzothioxanthene imide (S-DBI) and modified with a hydrophilic, bio-compatible polyoxyethylene (POE) side chain. In aqueous solution, owing to its amphiphilic character, DBI-POE self-assembles into nanoaggregates that disassemble upon binding to G4 DNA. This disassembly switches its photophysical behavior "turning on" its fluorescence while enabling two-photon near-infrared (NIR) excitation. Moreover, while DBI-POE follows a type I pathway in the aggregated state, producing superoxide anion ($O_2^{\bullet -}$) and hydroxyl ($OH^{\bullet}$) radicals, it shifts to a type II mechanism that predominantly generates singlet oxygen ($^1O_2$) upon G4 binding. The generated $^1O_2$ selectively oxidizes guanine residues, triggering G4 unfolding, a mechanism validated through biophysical experiments, dot blot assay and molecular dynamics (MD) simulations. Furthermore, biochemical experiments at single-base resolution reveal that photoactivated DBI-POE induces site-specific oxidative lesions at G4 sites, stalling DNA polymerase, while non-G4 regions remain unaffected. This combination of supramolecular disassembly, photophysical pathway switching, and G4-selective oxidative damage underscores the high specificity of DBI-POE, opening new avenues for the design of next-generation G4-targeted PSs for photodynamic cancer therapies.

New concepts

This pioneering study explores, for the first time, the mechanistic and dynamic basis of photodamage in G-quadruplex (G4) DNA structures, which are emerging as promising anticancer targets in photodynamic therapy. To this end, we designed **DBI-POE**, a hydrophilic, sulfur-substituted dibenzothioxanthene imide derivative derived from the most potent G4-specific photosensitizer reported, strategically modified with a neutral polyoxyethylene side chain to overcome the hydrophobic limitations of its precursor. In aqueous solution, **DBI-POE** self-assembles into aggregation-quenched nanostructures, with fluorescence restored upon selective binding and monomerization to G4 structures, a phenomenon termed disaggregation-induced emission. This transformation not only amplifies fluorescence intensity and extends excited-state lifetimes but also enables efficient two-photon excitation in the near-infrared region. Notably, the G4-induced disassembly shifts its photochemical pathway from a type I mechanism, characterized by superoxide and hydroxyl radical generation, to a guanine-selective type II mechanism that yields singlet oxygen exclusively. This precise switch triggers site-specific oxidative guanine lesions and complete G4 unfolding, as mapped by high-resolution DNA polymerase stop assays with single-base precision. Our multidisciplinary approach, integrating photochemistry, biophysics, biochemistry, quantum mechanical calculations, and molecular dynamics simulations, provides unprecedented mechanistic insights that pave the way for designing a brand-new generation of structure-specific, G4-targeted photosensitizers in anticancer phototherapy.

[a] *Institute of Advanced Materials, Faculty of Chemistry, Wrocław University of Science and Technology, Wyb. Wyspiańskiego 27, 50-370 Wrocław, Poland. E-mail: m.deiana@pwr.edu.pl*
[b] *Department of Microbial Genetics, Slovak Academy of Sciences, Institute of Molecular Biology, Dubravska cesta 21, 845 51 Bratislava, Slovakia*
[c] *Univ Angers, CNRS MOLTECH-ANJOU, SFR MATRIX, F-49000 Angers, France. E-mail: clement.cabanetos@univ-angers.fr*
[d] *Department of Chemistry, Universidad Autónoma de Madrid, Calle Francisco Tomás y Valiente, 7, 28049 Madrid, Spain*
[e] *IADCHEM, Institute for Advanced Research in Chemistry, Universidad Autónoma de Madrid, Calle Francisco Tomás y Valiente, 7, 28049 Madrid, Spain*
[f] *ENS de Lyon, CNRS, Laboratoire de Chimie, UMR 5182, 46 allée d'Italie, F-69342 Lyon, France*
[g] *Departamento de Química Física de Materiales, Instituto de Química Física Blas Cabrera, CSIC 28006, Madrid, Spain. E-mail: lmartinez@iqf.csic.es*

† Electronic supplementary information (ESI) available: Materials, experimental procedures, synthesis, characterization, photostability and aggregation studies, G4-binding interactions, absorption, emission, time-resolved fluorescence (TCSPC), two-photon absorption, singlet oxygen spectra, ABDA bleaching experiments, molecular docking, quantum mechanical calculations, and molecular dynamics simulations. See DOI: **https://doi.org/10.1039/d5nh00237k**

Introduction

Light-activated therapies have rapidly emerged as a transformative approach in oncology, offering the unprecedented ability to confine cytotoxic events with exquisite spatiotemporal control.[1–3] This precision minimizes systemic toxicity while maximizing therapeutic efficacy.[4] Among these approaches, photodynamic therapy (PDT) harnesses photosensitizers (PSs) that, upon illumination, generate reactive oxygen species (ROS) to induce localized oxidative stress and cell death.[2] Despite their promise, next-generation PSs face significant challenges, including aggregation in physiological media, suboptimal optical properties for deep-tissue penetration, and undesirable off-target interactions.[5,6] In particular, the development of heavy-atom-free PSs with superior photostability, selective accumulation, and robust ROS generation, preferentially in the near-infrared (NIR) therapeutic window, remains a critical objective.[7,8]

A compelling strategy to overcome these challenges involves the use of supramolecularly responsive systems.[9–13] While aggregation-induced emission (AIE) strategies have enhanced the photophysical performance of certain luminophores,[14–18] many conventional PSs suffer from aggregation-caused quenching (ACQ),[18–24] which diminishes their optical output and therapeutic efficiency. Recently, disaggregation-induced emission (DIE) approaches have been advanced to reverse ACQ effects in biological settings, thereby simultaneously amplifying fluorescence, improving bioavailability, and increasing therapeutic potency.[18,25]

Within this framework, G-quadruplex (G4) DNA has emerged as a potent trigger for controlled disassembly.[26–32] Imaging studies using G4-specific antibodies such as BG4,[33,34] alongside fluorescent reporters,[35,36] have provided direct evidence of G4 DNA formation in living cells. These structures are particularly enriched during the S phase of the cell cycle, suggesting a functional role in DNA replication.[33] Their formation is thought to be facilitated by duplex unwinding, which helps relieve thermodynamic strain.[37]

Computational analyses have predicted over 300 000 potential G4-forming sequences in the human genome,[38] while experimental approaches such as G4-seq have identified more than 700 000 G4 DNA sites,[39] including many that are not computationally predictable. Chromatin immunoprecipitation with BG4 followed by high-throughput sequencing (G4 ChIP-seq) has mapped G4 structures *in vivo*, revealing strong concordance with G4-seq data.[40]

Studies in immortalized human epidermal keratinocyte HaCaT cells have shown increased G4 levels in certain tissues compared to healthy controls.[40] Furthermore, G4 abundance has been reported to be significantly higher in cancer cells with impaired DNA repair mechanisms, such as triple-negative breast cancer (TNBC) cells, highlighting a potential link between genomic instability and G4 accumulation.[33] Overall, these findings indicate that G4s are predominantly located in regulatory regions, nucleosome-depleted zones, and promoters of actively transcribed genes in cancer cells, highlighting their key roles in gene regulation and genome organization.[40–42]

The physiological relevance of G4s is further supported by G4-interacting proteins, such as helicases.[43] These helicases unwind G4 structures to ensure proper DNA replication and transcription.[44,45] Mutations or loss of function in these helicases disrupt G4 resolution, leading to transcriptional dysregulation and genomic instability, hallmarks of cancer.[42]

The evidence that G4 DNA folds in a temporally regulated manner *in vivo*, and that these structures are concentrated in oncogenes and cancer-related genes, supports their relevance as targets for anticancer therapeutics.[46–49]

Beyond their regulatory roles in oncogene regulation,[41,42,50–52] G4s are also inherently prone to oxidation.[53–56] Since, among all nucleobases, singlet oxygen ($^1O_2$) preferentially oxidizes guanine residues,[57,58] G4 motifs are ideal targets for selective oxidative disruption.[53] However, despite this promise, only a handful of G4 targeting-PS structures have been developed, primarily operating *via* a type I mechanism.[59–64] In those rare instances, the molecular details of G4 oxidation remain unclear, as it is well established that type I radicals such as hydroxyl ($OH^\bullet$), generally react non-selectively with nucleobases.[58,65] For example, Chen *et al.* employed an acridinium derivative to target RNA G4s while generating superoxide anion ($O_2^{\bullet-}$) and $OH^\bullet$ radicals.[59] Similarly, Holden *et al.* used a Ru(II) complex to induce photodamage in mitochondrial G4s, although this compound failed to distinguish between G4 and duplex DNA.[63] In studies with supercoiled pUC19 plasmid DNA, light-induced cleavage persisted even in the presence of the $^1O_2$ trap sodium azide (NaN_3), suggesting involvement of multiple ROS.[63] Additionally, Zhang *et al.* reported that a triazole-attached dibenzoquinoxaline targeting G4 motifs produces $O_2^{\bullet-}$ and $OH^\bullet$ radicals, but not $^1O_2$.[60]

Clearly, although previous studies have advanced our understanding of PS-mediated phototherapy at both cellular and *in vivo* levels, they have not yet clarified the molecular mechanisms underlying selective G4 damage.

In our earlier work, we demonstrated that heavy-atom-free mono-(**BTI**) and dibenzothioxanthene (**DBI**) PSs exhibited potent phototherapeutic activity with negligible dark toxicity.[66–71] Notably, sulfur-substituted **S-DBI** showed exceptional G4-binding affinity and nearly unitary $^1O_2$ generation quantum efficiency.[67] However, its intrinsic hydrophobicity resulted in significant aggregation in aqueous solution, complicating detailed mechanistic studies of its G4-mediated phototherapeutic action.[67]

To address these challenges, gain deeper insights into selective G4 targeting, and ultimately facilitate future clinical translation, we developed **DBI-POE**, an amphiphilic, heavy-atom-free PS derived from **S-DBI** and modified with a hydrophilic polyoxyethylene (POE) side chain (Scheme 1). In aqueous media, **DBI-POE** spontaneously self-assembles into well-defined nanoaggregates that disassemble upon selective binding to G4 DNA. This disassembly not only activates the PS's emissive properties and two-photon absorption but also reprograms its photophysical behavior from a type I pathway, which produces $O_2^{\bullet-}$ and $OH^\bullet$ radicals, to a type II pathway that predominantly generates $^1O_2$.

Comprehensive biophysical and theoretical studies, including circular dichroism (CD), nuclear magnetic resonance (NMR), molecular dynamics (MD) simulations and quantum mechanical (QM) calculations, confirmed that the photoinduced $^1O_2$

selectively oxidized guanine residues, triggering precise unfolding of the G4 structure. Moreover, primer extension assays at single-base pair resolution revealed that photoactivated **DBI-POE** induced site-specific oxidative lesions that stalled DNA polymerase exclusively at damaged G4 regions, while, critically, non-G4 sequences remained unaffected.

Results and discussion

Photosensitizer design and characterization

Previously, we demonstrated that **S-DBI** exhibits exceptional G4-binding affinity and potent photodynamic therapeutic effects across 2D and 3D cancer cell models, as well as in a zebrafish rhabdomyosarcoma model.[67,72] However, the intrinsic propensity of this compound to form highly stable nanoaggregates has impeded detailed mechanistic investigations into its phototriggered oxidative DNA damage at G4 sites (Scheme 1).

To overcome this limitation and, for the first time, elucidate the molecular basis of G4-mediated photodynamic performance, we designed and synthesized **DBI-POE**, a hydrophilic variant of **S-DBI** modified with a polyoxyethylene (POE) side chain. **DBI-POE** was synthesized *via* a straightforward route starting from the previously prepared compound **DBA** (Scheme 1 and Fig. S1–S3, ESI†).[67] As expected, the introduction of the POE substituent significantly enhances solubility by approximately 4.0-fold and reduces aggregation under biologically relevant conditions (*vide infra*).

In organic solvents such as methanol (MeOH)[22,31] and dimethyl sulfoxide (DMSO),[26,27] both recognized for their strong solubilizing and disaggregating properties, **DBI-POE** exhibited a sharp absorption band at approximately 485 nm (Fig. S4 and S5, ESI†). This observation aligns with computational predictions ($S_1(\pi\pi^*)$ state of **DBI-POE**, oscillator strength of 0.59, at 2.99 eV [413 nm], Table S4, ESI†) and closely mirrors the spectral characteristics of its sulfur-substituted parent structure in organic solvents, clearly indicating that the compound is well dissolved in these high polarity solvents.[67] Upon incremental water addition, this absorption band gradually decreased in intensity, broadened, and underwent a bathochromic shift ($S_1(\pi\pi^*)$ state of the dimer **DBI-POE$_2$**, oscillator strength of 0.03, at 2.89 eV [429 nm], Table S4 (ESI†), being the spectroscopic state S_2), indicative of a self-assembly process driven by interchromophoric interactions reminiscent of slip-stacked arrangement (Fig. S4 and S5, ESI†).[30,73] Concomitantly, fluorescence studies in pure MeOH revealed an emission band centered at 551 nm that experienced approximately a five-fold quenching and a shift to 564 nm with increasing water content, pointing to the existence of competitive less emissive or non-radiative decay pathways (Table S5 and Fig. S4B, ESI†).[22]

The UV/vis and emission spectra of **DBI-POE**, recorded in MeOH or in cell culture medium supplemented with 10% fetal calf serum after exposure to 485 ± 20 nm light for 1 hour at an irradiance of 10 mW cm^{-2}, demonstrated excellent photostability, an essential prerequisite for effective long-term photosensitization (Fig. S6, ESI†).

Temperature-dependent UV/vis and emission experiments further underscored the reversible nature of **DBI-POE** self-assembly in aqueous media: at 25 °C, the dye exhibited broad absorption and quenched emission, whereas at 95 °C, it reverted to a well-defined absorption profile with progressively enhanced emission (Fig. S7, ESI†).[28] Moreover, the addition of the anionic surfactant sodium dodecyl sulfate (SDS), widely

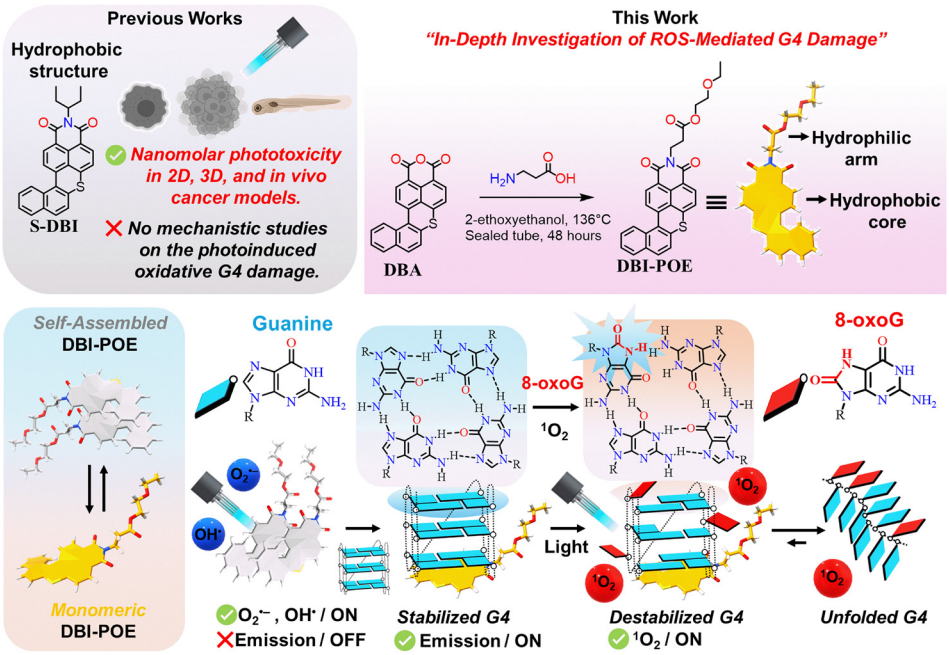

Scheme 1 Structural limitations of **S-DBI**, which prevented detailed mechanistic studies of mediated photoinduced oxidative G4 damage. Synthetic pathway for **DBI-POE**, highlighting its unique structural features compared to **S-DBI** (this work), and demonstration of how **DBI-POE** targets G4 structures, triggering a transformative shift from type I to type II mechanisms, and ultimately induces oxidative G4 damage (bottom panel).

used as a disaggregating agent to facilitate the dispersion and solubilization of aggregated compounds, induced pronounced changes in both the absorption and emission spectra, consistent with the disassembly of **DBI-POE** aggregates into monomeric species (Fig. 1A).[26–29] Dynamic light scattering (DLS) measurements corroborated these spectroscopic findings by revealing the formation of uniform **DBI-POE** nanoaggregates with an average diameter of 190 nm in aqueous media (Fig. 1B). Calculations predicted the formation of the most stable dimeric species (**DBI-POE$_2$**), with an aggregation free energy of −4.6 kcal mol^{-1} (Fig. 1C, Fig. S22 and Table S3, ESI†).

Collectively, these results confirm the reversible aggregation behavior of **DBI-POE** and highlight its potential for further sensing applications through modulation of its photophysical properties.

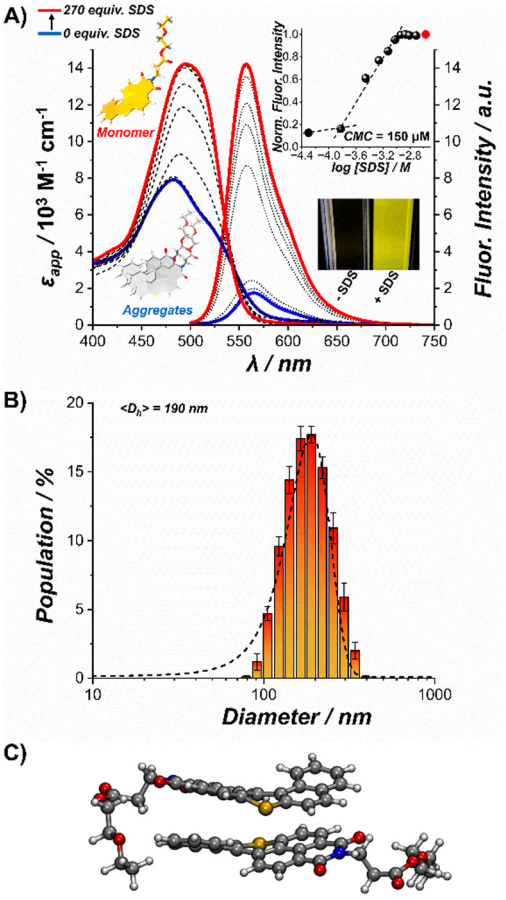

Fig. 1 (A) UV/vis absorption and emission spectral changes of **DBI-POE** measured in the absence (blue line) and presence (black and red lines) of SDS (**DBI-POE** = 10 μM and SDS = 0–2.7 mM in 50 mM Tris, pH 6.8, λ_{exc} = 450 nm). Insets show the emission spectral changes monitored at λ_{em} = 557 nm as a function of SDS concentration, revealing a critical micelle concentration (CMC) of 150 μM and the associated color changes resulting from aggregate-to-monomer transitions under blue light irradiation. (B) DLS measurements of **DBI-POE** (3.5 μM) in aqueous solution, demonstrating the formation of nanoaggregates. N = 3; error bars indicate the mean ± SD. (C) Optimized ground state structure for **DBI-POE$_2$** species; carbon, sulfur, nitrogen, oxygen, and hydrogen atoms are shown in grey, yellow, blue, red, and white, respectively.

G4-mediated molecular disassembly and enhanced optical outputs

Encouraged by the activatable assembly–disassembly behavior of **DBI-POE**, we investigated its molecular recognition capacity toward G4 structures under physiologically relevant ionic conditions (100 mM K$^+$). In aqueous solution, **DBI-POE** exhibited its characteristic broad absorption band and low-intensity emission, with a lowered fluorescence quantum yield (Φ_F) of 4% (~10% in organic solvents),[67] which is indicative of dye self-assembly (Fig. 2A, Table 1 and Table S1, ESI†). Upon incremental addition of the *c-MYC* Pu22 sequence,[27,48,51] a well-established intramolecular parallel G4 structure (Fig. S25, ESI†), located in the *MYC* promoter and commonly used in structural studies to investigate ligand-binding interactions,[27,48,74] we observed a gradual increase in the absorption ($S_1(\pi\pi^*)$ state of **DBI-POE**:*c-MYC* Pu22, oscillator strength of 0.41, at 2.89 eV, Table S4, ESI†) accompanied by the emergence of two well-resolved isosbestic points (Fig. 2A). These spectral transitions signified the formation of a well-defined **DBI-POE**:*c-MYC* Pu22 complex that mirrored the optical behavior of **DBI-POE** observed in organic solvents (Fig. S4 and S5, ESI†), in the presence of SDS (Fig. 1A), or at elevated temperatures (Fig. S7, ESI†), thereby corroborating G4-mediated disaggregation.[25–29] These results are consistent with computational docking simulations, where the stacked dimer disaggregates upon G4 intercalation of one of the monomers, while the other monomer binds externally (see ESI† for details and Fig. S27). Concurrent fluorescence measurements revealed a progressive "turn-on" of emission, reaching a Φ_F of 15% at 5.0 equiv., which confirmed the conversion of weakly emissive nanoaggregates into emissive monomeric species (Fig. 2A and Table S1, ESI†). Indeed, the QM results for **DBI-POE** within the *c-MYC* Pu22 structure revealed the existence of just one emissive minimum, similar to that of the monomeric **DBI-POE** species (Table S5, ESI†).

Quantitative analysis using global nonlinear fitting of the emission data supported a 1:1 binding model, yielding an association constant (K_a) of 2.7 × 10^5 M^{-1} (Fig. 2B).[75] This value aligns with those reported for other G4 fluorescent probes,[29,31,52] including our own works on related **DBI** derivatives.[67,71] Job's plot analysis further confirmed the stoichiometry by showing saturation at a mole fraction of approximately 0.5 (Fig. S8, ESI†). This stoichiometry is preferred over higher-order complexes, which can lead to multiple ligands binding to the G4 template and uncontrolled photodamage.[48] To probe the specificity of this interaction, we expanded our studies to include a diverse panel of previously characterized G4 structures, including parallel (*c-MYC* Pu22; vascular endothelial growth factor, *VEGF*; hypoxia-inducible factor 1-alpha, *HIF*-1α), hybrid (Telomeric, Tel-23), and antiparallel (thrombin-binding aptamer, TBA) topologies, as well as non-G4 controls such as single-stranded (ss) and double-stranded (ds) DNA (Table S2, ESI†).[26,67] These G4 DNA structures were selected for their biological relevance and well-characterized folding topologies, representing the broad structural diversity that G4s can adopt.[48,76–79] Strikingly, only parallel G4 structures, and to a lesser extent, the hybrid conformation,

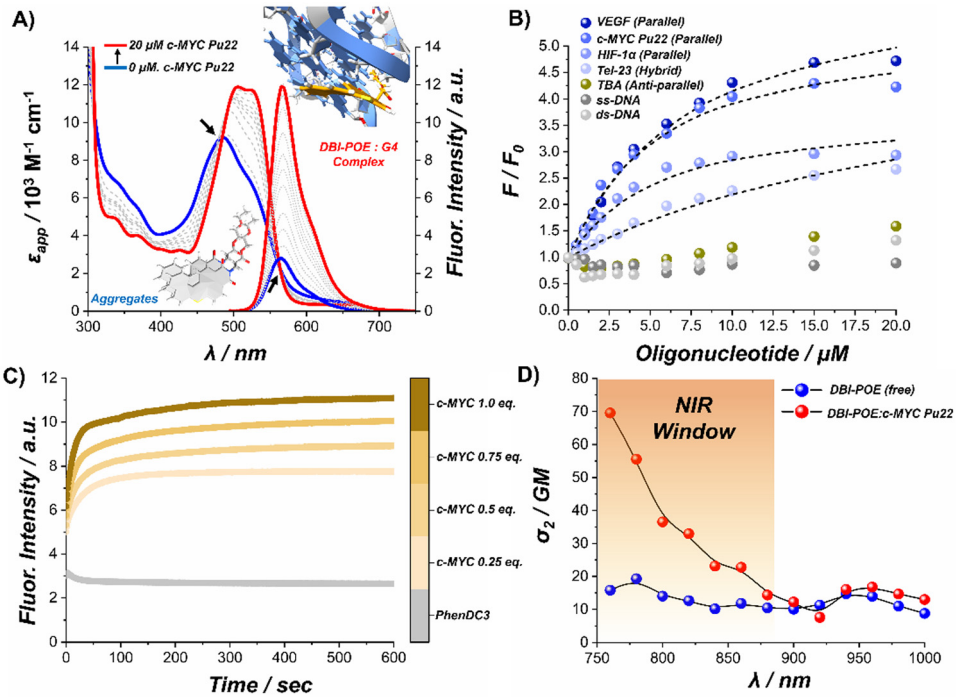

Fig. 2 (A) UV/vis absorption and steady-state fluorescence spectral changes upon complexation of **DBI-POE** (blue lines) with the parallel G4 DNA structure *c-MYC* Pu22 (gray and red lines). Measurements were performed using **DBI-POE** = 10 μM for absorption experiments and 2 μM for emission experiments, with *c-MYC* Pu22 titrated from 0 to 20 μM in 50 mM Tris (pH 6.8) containing 100 mM KCl (λ_{exc} = 485 nm). Solid arrows indicate the emergence of isosbestic points. (B) Binding isotherms from spectrofluorimetric titration assays using parallel, hybrid, antiparallel, and non-G4 DNA structures in 50 mM Tris, pH 6.8, 100 mM KCl (λ_{exc} = 485 nm). Dashed lines indicate 1 : 1 nonlinear fits obtained with the BindFit program. Data for the antiparallel and non-G4 DNA structures were not fitted due to the lack of a saturation profile even at high oligonucleotide concentrations. (C) Time-dependent competitive binding assay employing the benchmark G4 compound PhenDC3 (**DBI-POE** = 2.0 μM, *c-MYC* Pu22 = 0.5, 1.0, 1.5 or 2.0 μM and PhenDC3 = 5 μM in 50 mM Tris, pH 6.8, 100 mM KCl, λ_{exc} = 485 nm). (D) σ_2 values calculated by TPEF for free **DBI-POE** (blue dots) and for the **DBI-POE**:*c-MYC* Pu22 complex (**DBI-POE** = 5 μM and *c-MYC* Pu22 = 25 μM in 50 mM Tris, pH 6.8, 100 mM KCl). The black lines are for guidance only.

induced significant disassembly of **DBI-POE** aggregates, whereas antiparallel G4, ssDNA, and dsDNA produced minimal or no spectral changes (Fig. 2B, Fig. S9, S10 (ESI†) and Table 1). The absorption spectral changes observed during the titration of **DBI-POE** with either antiparallel G4 or non-G4 sequences likely result from a reorganization of **DBI-POE**'s supramolecular state, during which the oligonucleotides act as a crowder agent rather than engaging in the specific interactions that lead to complex formation (Fig. S9, ESI†).[26,29,30] This selectivity has also been observed for other G4-selective probes operating *via* DIE and likely arises from the accessible π-stacking surfaces of parallel G4s, which lack lateral or diagonal loops.[25,26,29,31,32] This compact architecture facilitates strong interactions with the aromatic core of **DBI-POE**. Complementary steady-state and time-dependent competition assays using the well-established G4 ligand PhenDC3[80–83] further confirmed the specific binding of **DBI-POE** to *c-MYC* Pu22 (Fig. 2C, Fig. S11 and Scheme S1, ESI†). In these assays, PhenDC3's high affinity for the *c-MYC* Pu22 G4 directly competes with **DBI-POE** for the same binding site. As a result, **DBI-POE** is displaced, leading to a significant drop in its emission intensity. This observation reinforces the notion that **DBI-POE** interacts specifically with the G4 structure and that its binding is reversible and competitive, as evidenced by its displacement by PhenDC3.

Time-correlated single-photon counting (TCSPC) measurements provided additional mechanistic insights. They revealed that parallel G4 structures (*c-MYC* Pu22 or *HIF-1α*) significantly extended **DBI-POE**'s fluorescence lifetime by reducing non-radiative decay (k_{nr}) and enhancing radiative decay (k_r) (Fig. S12 and Table 1, Table S1, ESI†). In contrast, antiparallel G4 and non-G4 sequences had minimal effects, indicating that parallel G4 binding effectively suppresses non-radiative pathways and boosts both emission intensity and excited-state lifetime.

Two-photon excited fluorescence (TPEF) studies demonstrated that while unbound **DBI-POE** exhibited a modest two-photon absorption cross section (σ_2 = 15.8 GM at 760 nm), its complexation with *c-MYC* Pu22 increased this value by a factor of approximately 4.5, thereby enabling effective photosensitization of the dye in the biologically favorable first NIR window (Fig. 2D and Table 1).[28] In line with our above mentioned disassembly experiments, this enhancement was much less pronounced (~two-fold) when **DBI-POE** was incubated with the antiparallel G4 TBA or ds-DNA (Fig. S13 (ESI†) and Table 1). NIR light (700–1000 nm) offers deeper tissue penetration, reduced scattering and absorption, and minimal photodamage, while its confined excitation minimizes off-target effects, potentially enhancing tumor targeting when **DBI-POE** binds to *c-MYC* G4.[84] Although promising, two-photon G4-interactive compounds are still in

Table 1 Summary of the binding constants and spectroscopic properties of **DBI-POE** either free or complexed with G4 and non-G4 DNA structures

System	Topology[a]	K_a[b]/M^{-1}	λ_{em}/nm	Φ_F[d]/%	$\langle\tau\rangle$/ns	$k_r/10^6$ s^{-1}	$k_{nr}/10^6$ s^{-1}	σ_2[f]/GM	Φ_Δ/%
DBI-POE	—	—	565	4[e]	3.4	13.0	281.5	15.8	84[g]/72[g]
c-MYC Pu22	P	2.7×10^5	566	11[e]	5.2	20.2	170.8	69.5	22[h]
HIF-1α	P	2.7×10^5	568	9[e]	4.3	24.4	206.6	—	—
VEGF	P	1.8×10^5	567	—	—	—	—	—	—
Tel-23	H	4.6×10^4	565	—	—	—	—	—	—
TBA	AP	ND[c]	566	6[e]	3.5	16.6	268.0	30.6	—
ss-DNA	NG4	ND[c]	566	5[e]	3.3	15.4	287.0	ND	—
ds-DNA	NG4	ND[c]	566	6[e]	3.6	15.8	263.6	28.5	—

[a] Topological structure, P = parallel, H = hybrid, AP = antiparallel, and NG4 = non-G4 structure. [b] Data fitting to a 1 : 1 binding model on the fluorimetric titration data was performed using Bindfit, which employed multiple global fitting methods (Nelder–Mead method). [c] Not determined (ND) due to the absence of a saturation binding profile. [d] Fluorescein is used as the reference standard (0.1 M NaOH, Φ_F = 0.93). [e] Φ_F was calculated in 50 mM Tris buffer (pH 6.8) containing 100 mM KCl at 25 °C. All values are reported for a 1 : 1 **DBI-POE**/oligonucleotide ratio. See Table S1 (ESI) for additional data. [f] Fluorescein is used as the reference standard (0.1 M NaOH). [g] Determined by direct $^1O_2$ phosphorescence method in EtOH or MeOH using Rose Bengal in MeOH as the reference standard ($\Phi_{\Delta(RB)}$ = 0.76). [h] Determined by ABDA bleaching experiments using Methylene Blue in water as the reference standard ($\Phi_{\Delta(MB)}$ = 0.52). Experiments are reported for a 1 : 1 **DBI-POE**/*c-MYC* Pu22 ratio in 50 mM Tris buffer (pH 6.8) containing 100 mM KCl at 25 °C.

their infancy.[28,85,86] Our data indicate that **DBI-POE** is a promising scaffold for two-photon PDT, as G4-triggered disaggregation significantly enhances its emissive properties and σ_2, thereby increasing its two-photon brightness ($\Phi_F \times \sigma_2$)[28,87] and enabling advanced imaging and phototherapeutic strategies targeting oncogene promoter regions.

G4-driven type I-to-type II photophysical conversion

The generation of reactive triplet states is an essential prerequisite for initiating either type I or type II photochemical mechanisms. We have then estimated the intersystem crossing (ISC) probability for **DBI-POE**, **DBI-POE$_2$**, and **DBI-POE**:*c-MYC* Pu22 complex by computing spin–orbit coupling (SOC) terms at the position of the minimum-energy geometry in the S_1 electronic state ($S_{1\,min}$). The **DBI-POE**:*c-MYC* Pu22 complex exhibits larger SOCs for the closest triplet in energy from S_1 (Table S6, ESI†), being almost double that of **DBI-POE**. Having established that the triplets can be potentially populated, we systematically evaluated the ROS-generating potential of **DBI-POE** by NIR $^1O_2$ phosphorescence measurements in MeOH and ethanol (EtOH), solvents in which **DBI-POE** is highly soluble (Fig. S14, ESI†).[67,88] In EtOH, **DBI-POE** exhibited a high singlet oxygen quantum yield (Φ_Δ = 84%), consistent with the almost unitary values found for its lipophilic counterpart **S-DBI** in chloroform.[67] In comparison, a decreased yield is found in MeOH (Φ_Δ = 72%). It should be noted that direct detection of $^1O_2$ *via* its phosphorescence band is inherently limited by low sensitivity, particularly in aqueous media. Consequently, **DBI-POE** alone or in its complex with *c-MYC* Pu22 in aqueous solution did not yield a sufficiently strong signal, making direct $^1O_2$ detection impractical and necessitating the use of alternative assays.

To overcome this limitation, we employed 9,10-anthracenediyl-bis(methylene)dimalonic acid (ABDA) as a specific water-soluble $^1O_2$ sensor.[89] ABDA can be readily oxidized to an endoperoxide by $^1O_2$, resulting in a decrease in its absorption that can be easily tracked by UV/vis spectroscopy.[89] Under our irradiation protocol, ABDA alone or in the presence of either **S-DBI** or the **S-DBI**:*c-MYC* Pu22 complex exhibited negligible spectral changes (Fig. S15, ESI†). In contrast, exposure to **DBI-POE** led to progressive ABDA bleaching, indicating effective photoinduced ROS production (Fig. 3A). Notably, the addition of the *c-MYC* Pu22 G4 sequence resulted in a comparable ABDA bleaching profile, demonstrating that **DBI-POE** retains good ROS-generating capability even when bound to G4 structures (Fig. 3A). This effect was found to be independent of the *c-MYC* Pu22 concentration (Fig. S16, ESI†).

Under oxygen-depleted conditions, neither free **DBI-POE** nor its *c-MYC* Pu22 complex induced significant ABDA bleaching, confirming the oxygen-dependent nature of the process, and its dependency on ROS generation (Fig. S17, ESI†).

To determine the chemical nature of the generated ROS, we introduced NaN_3, a well-established $^1O_2$ quencher.[89] To our surprise, NaN_3 completely suppressed ABDA bleaching only in samples containing the **DBI-POE**:*c-MYC* Pu22 complex, whereas it had no effect on free **DBI-POE**, even at elevated concentrations, pointing to a predominant type I pathway (likely involving $O_2^{\bullet-}$ or $OH^\bullet$ species) for the free dye and a type II mechanism (selective for $^1O_2$) upon G4 binding (Fig. 3B and Fig. S18, ESI†). Based on this premise, we calculated a Φ_Δ of 22% from ABDA bleaching for the **DBI-POE**:*c-MYC* Pu22 complex, a significant value for phototherapeutic applications.[68] Substituting *ds*-DNA for *c-MYC* Pu22 again led to NaN_3-insensitive bleaching, as observed for free **DBI-POE**, highlighting the critical role of the G4 conformation in eliciting $^1O_2$ production (Fig. S19, ESI†).

To further investigate the generation of $^1O_2$ by **DBI-POE** when bound to *c-MYC* Pu22, we conducted ABDA bleaching experiments in a buffered solution containing 85% deuterium oxide (D_2O). Since, opposite to NaN_3, D_2O extends the lifetime of $^1O_2$, we anticipate that it should amplify ABDA bleaching and thus provide direct evidence of $^1O_2$ involvement.[89] Indeed, in D_2O, the **DBI-POE**:*c-MYC* Pu22 complex exhibited a two-fold increase in ABDA bleaching rate, which was completely suppressed by NaN_3, whereas free **DBI-POE** remained robustly insensitive to both D_2O and NaN_3 (Fig. 3A and B). Together, these observations indicate that complexation with *c-MYC* Pu22 shifts **DBI-POE** from a type I to a type II photochemical pathway, which constitutes to the best of our knowledge an unprecedented observation.

To explore the reversibility of G4 binding and its direct influence on ROS generation, we conducted competitive

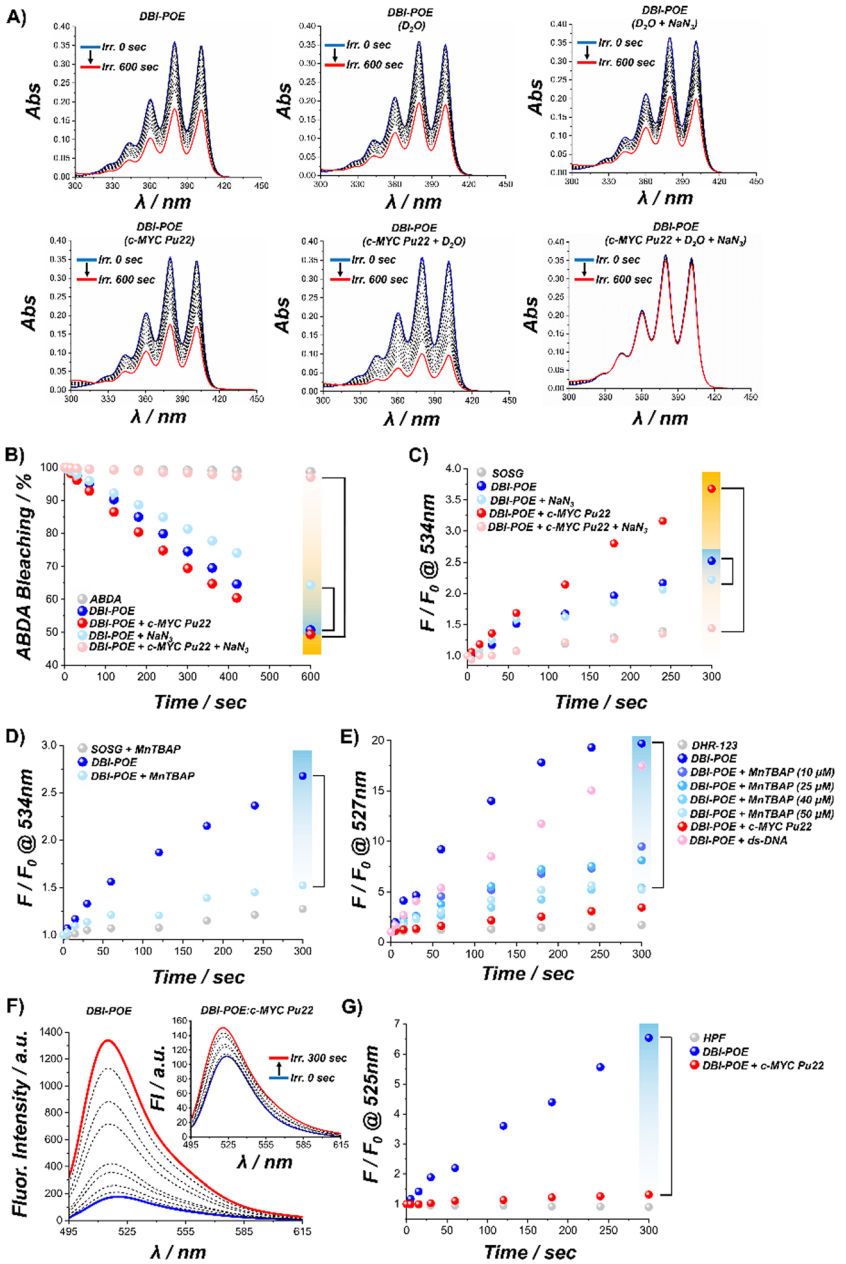

Fig. 3 (A) ABDA bleaching experiments under various conditions. Samples contained ABDA = 30 μM, NaN_3 = 10 mM, **DBI-POE** = 5 μM, and *c-MYC* Pu22 = 5 μM in 50 mM Tris (pH 6.8) with 100 mM KCl. Where indicated, D_2O was used in place of H_2O. (B) ABDA bleaching at 380 nm expressed as a percentage, showing that NaN_3 had negligible effects on **DBI-POE** alone but fully scavenged the **DBI-POE**:*c-MYC* Pu22 complex. (C) SOSG fluorescence enhancement under similar conditions: SOSG = 10 μM, NaN_3 = 10 mM, **DBI-POE** = 5 μM, and *c-MYC* Pu22 = 5 μM in 50 mM Tris (pH 6.8) with 100 mM KCl, λ_{exc} = 488 nm (D) SOSG fluorescence enhancement mediated by **DBI-POE** was quenched by MnTBAP = 50 μM. (E) DHR-123 fluorescence enhancement under varying conditions: DHR-123 = 10 μM, MnTBAP = 0–50 μM, **DBI-POE** = 5 μM, *c-MYC* Pu22 = 5 μM, and ds-DNA = 5 μM in 50 mM Tris (pH 6.8) with 100 mM KCl, λ_{exc} = 488 nm. In all experiments, irradiation was performed at 485 ± 20 nm at an irradiance of 10 mW cm^{-2} over various time intervals. (F) Fluorescence enhancement of HPF (5 μM) in the presence of **DBI-POE** (5 μM), or in complex with *c-MYC* Pu22 (5 μM) as shown in the inset. (G) Fold change in HPF fluorescence under different conditions: HPF = 5 μM, **DBI-POE** = 5 μM, *c-MYC* Pu22 = 5 μM, in 50 mM Tris (pH 6.8) with 100 mM KCl, λ_{exc} = 490 nm. In all experiments, irradiation was performed at 485 ± 20 nm at an irradiance of 10 mW cm^{-2} over various time intervals.

displacement assays using PhenDC3 (*vide supra*). Under strongly competitive conditions (PhenDC3 = 25 μM), **DBI-POE** was displaced from the *c-MYC* Pu22 template, restoring its self-assembly and NaN_3-resistant photosensitization properties, as seen from ABDA bleaching profile (Fig. S20A, ESI†). At lower PhenDC3 concentrations (1 μM), the complex remained largely intact, and NaN_3-sensitive bleaching persisted (Fig. S20B, ESI†).

Additionally, we performed scavenger studies using mannitol,[90] sodium pyruvate,[91] and the superoxide dismutase mimetic manganese(III)tetrakis(4-benzoic acid)porphyrin (MnTBAP),[92] which are

selective for $OH^{\bullet}$ radicals,[90] hydrogen peroxide (H_2O_2),[91] and $O_2^{\bullet-}$,[92] respectively. Among the tested scavengers, MnTBAP stood out for its ability to significantly reduce ABDA bleaching induced by free **DBI-POE** under conditions where NaN_3 had no effect, confirming the involvement of $O_2^{\bullet-}$ in its photochemical pathway (Fig. S21, ESI†).

Complementary experiments using Singlet Oxygen Sensor Green (SOSG),[93] as an additional $^1O_2$ control probe, revealed that both free **DBI-POE** and its *c-MYC* Pu22 complex activated SOSG fluorescence, albeit to different extents (Fig. 3C). Notably, only the fluorescence enhancement in the G4-bound state was suppressed by NaN_3, consistent with exclusive $^1O_2$ production (Fig. 3C). Moreover, in agreement with the ABDA studies, MnTBAP significantly reduced the SOSG emission enhancement induced by **DBI-POE**, supporting the generation of $O_2^{\bullet-}$ radicals (Fig. 3D).

It has been well documented that ABDA and SOSG exhibit high specificity for $^1O_2$ compared to other ROS, with minimal off-target interactions reported.[89] However, our findings underscore the importance of employing an extensive array of control experiments when utilizing ROS probes. Such rigorous cross-control is essential to accurately assess the specificity of the generated ROS and to discard false-positive results.

Next, we hypothesized that free **DBI-POE** and its *c-MYC* Pu22-bound complex would exhibit contrasting photophysical responses when probed with $O_2^{\bullet-}$-specific sensors. To test this, we employed dihydrorhodamine-123 (DHR-123), a non-fluorescent compound that is oxidized to the highly fluorescent rhodamine-123 upon exposure to $O_2^{\bullet-}$ radicals.[11,94] The DHR-123 assays revealed that free **DBI-POE** induced a strong fluorescence response, indicative of robust $O_2^{\bullet-}$ generation (Fig. 3E). In contrast, the **DBI-POE**:*c-MYC* Pu22 complex elicited minimal DHR-123 activation, suggesting that G4 binding suppresses $O_2^{\bullet-}$ production (Fig. 3E). Control experiments with *ds*-DNA instead of *c-MYC* Pu22 produced DHR-123 activation levels comparable to those of free **DBI-POE** (Fig. 3E). Furthermore, the addition of increasing concentrations of MnTBAP resulted in a dose-dependent decrease in DHR-123 fluorescence, thereby confirming that free **DBI-POE** generates $O_2^{\bullet-}$ radicals (Fig. 3E).

Further evidence was obtained using the $OH^{\bullet}$-selective fluorescent probe hydroxyphenyl fluorescein (HPF), which specifically emits fluorescence upon reaction with $OH^{\bullet}$ radicals.[11] Free **DBI-POE** strongly induced HPF fluorescence, indicating efficient $OH^{\bullet}$ generation through a type I photochemical pathway. In contrast, the **DBI-POE**:*c-MYC* Pu22 complex exhibited minimal HPF fluorescence enhancement, highlighting the shift toward a predominantly $^1O_2$-mediated photochemical mechanism (Fig. 3F and G).

Collectively, these findings establish **DBI-POE** as the first example of a supramolecular, G4-specific PS capable of toggling between two distinct photophysical pathways, type I and type II, depending on its aggregation state and G4 binding. This G4-induced disassembly not only enables robust $^1O_2$ production, which preferentially oxidizes guanine residues, but also significantly enhances the prospects for targeted PDT that exploit the unique structural and electronic features of G4 motifs.

Light-mediated G4 unfolding and site-specific oxidative guanine damage

To elucidate the effect of photogenerated $^1O_2$ by **DBI-POE** on the G4 scaffold, we employed a multi-technique approach that integrates spectroscopic, biochemical, and computational methods.

Initially, CD spectroscopy was used to monitor structural changes in the *c-MYC* Pu22 sequence. In the absence of **DBI-POE**, the G4 exhibited the expected CD spectral features characterized by a positive peak at ~260 nm and a negative peak at ~240 nm (Fig. 4A).[48,52,95] When **DBI-POE** was added in the dark, only minimal spectral alterations were observed, akin to those induced by other uncharged G4-binding compounds.[26–28] However, exposure to light produced a dose-dependent decrease in CD band intensity, ultimately yielding a spectrum suggestive of an unfolded G4 (Fig. 4A).[96] These results suggest that photoactivation of **DBI-POE** leads to guanine oxidation and subsequent G4 disruption.[97]

Complementary ^1H NMR spectroscopy further corroborated these findings. The free *c-MYC* Pu22 oligonucleotide displayed the expected 12 imino proton resonances associated with G4 formation (Fig. 4B).[48,51] While dark-incubated **DBI-POE** caused only slight spectral changes, with a moderate broadening of the peaks, light irradiation resulted in a progressive disappearance of these imino signals, confirming a light-dependent unfolding of the G4 structure (Fig. 4B).

Thermal stability assessments *via* temperature-dependent CD melting assays provided additional insight on the photodegradation mechanism (Fig. 4C). Under control conditions, *c-MYC* Pu22 demonstrated high thermal stability ($T_{m(c\text{-}MYC\ Pu22)}$ = 69 °C). Notably, **DBI-POE** in the dark increased the melting temperature by ~8 °C ($T_{m(\mathbf{DBI\text{-}POE}:c\text{-}MYC\ Pu22)}$ = 77 °C), reflecting the stabilizing influence of **S-DBI**.[67] In stark contrast, light activation of **DBI-POE** reduced the melting temperature by ~40 °C ($T_{m(\mathbf{DBI\text{-}POE}:c\text{-}MYC\ Pu22\ +\ Light)}$ = 37 °C) decisively indicating that photooxidative damage, most likely mediated by guanine oxidation, disrupts the tetrad integrity essential for G4 stability.

Indeed, docking followed by MD simulations also support these findings, as **DBI-POE** stabilizes the G4 structure in its most favorable pose in the dark (Fig. 4D and S28, see ESI† for details), while the oxidized G4 becomes disrupted upon light exposure (Fig. S29, ESI†).

Control experiments, where *c-MYC* Pu22 was exposed to light irradiation in the absence of **DBI-POE**, resulted in no spectral alterations.

In line with our observations, previous studies have demonstrated that oxidative lesions, such as 8-oxo-7,8-dihydroguanine (8-oxoG), generally impair the hydrogen-bonding capacity of guanine, often leading to a loss of G4 structure.[98] However, notable exceptions exist.[99] For example, the Burrows group reported that an additional guanine track in oncogene promoter G4 sequences can serve as a ''spare tire,'' helping to preserve the G4 fold under oxidative stress.[100] Similarly, the Opresko lab showed that telomeric G4 sequences containing a single 8-oxoG mutation retained their hybrid conformation, although the binding affinity of the G4-specific antibody BG4[33] was reduced depending on the lesion's precise location.[101]

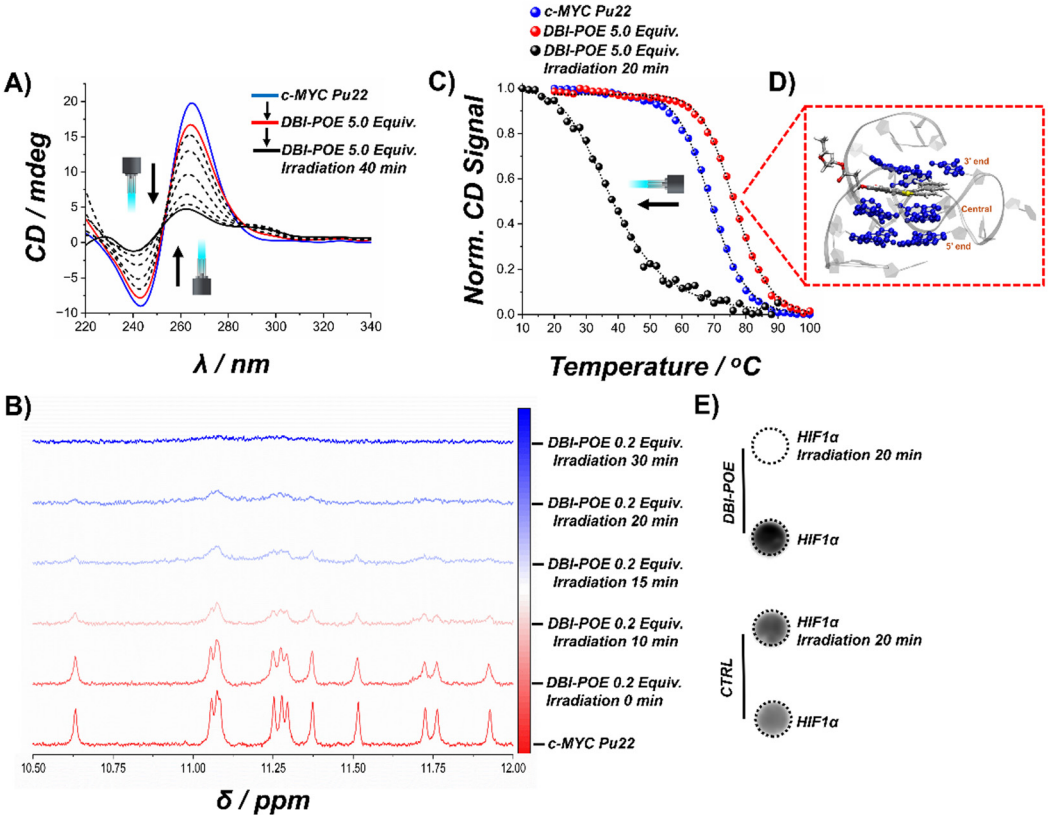

Fig. 4 (A) CD spectra of *c-MYC* Pu22 recorded in the absence and presence of **DBI-POE**. Measurements were performed using *c-MYC* Pu22 = 2 μM and **DBI-POE** = either 0 or 10 μM in 50 mM Tris buffer (pH 6.8) containing 100 mM KCl. (B) ^{1}H NMR spectra of *c-MYC* Pu22 recorded in the absence and presence of **DBI-POE**. Measurements were performed using *c-MYC* Pu22 = 200 μM and **DBI-POE** = either 0 or 40 μM in 50 mM Tris buffer (pH 6.8) containing 100 mM KCl. (C) CD-based melting profiles of *c-MYC* Pu22 recorded in the absence and presence of **DBI-POE**, plotted at the CD maximum at 264 nm. Measurements were performed using *c-MYC* Pu22 = 2 μM and **DBI-POE** = either 0 or 10 μM in 50 mM Tris buffer (pH 6.8) containing 5 mM KCl. (D) Representative MD structure of **DBI-POE** stable poses from the dbscan clustering of the last 1 μs of the MD production. (E) Dot blot assay was performed using *HIF*-1α = 8 μM and **DBI-POE** = either 0 or 8 μM in 10 mM Tris buffer (pH 7.4) containing 100 mM KCl. (A–C) Irradiation was carried out at 485 ± 20 nm at an irradiance of 10 mW cm^{-2} over various time intervals. (E) Irradiation was carried out at 460–495 nm for 20 min. DMSO was used as a control in all experiments.

Therefore, to further validate the impact of oxidative damage mediated by **DBI-POE**, we performed immuno dot blot assays using BG4 (Fig. 4E). In our hands, the *c-MYC* Pu22 sequence was poorly recognized by BG4 resulting in a weak signal. Therefore, we employed the *HIF*-1α G4 sequence, which is effectively targeted by both BG4 and **DBI-POE** (Fig. 2B).[67] Control samples maintained BG4 targeting capability, as evidenced by a robust immunosignal in the dot blot assay, whereas light-activated **DBI-POE** led to significant disruption of the G4 structure, accompanied by a marked decrease in BG4 binding, a clear hallmark of oxidative damage.

Our experiments clearly demonstrate that **DBI-POE**'s ability to generate $^{1}O_2$ efficiently damages the G4 structure, resulting in its complete destabilization and unfolding.

To reconstitute *in vitro* DNA replication across a G4-containing template, we used a primer extension assay that faithfully mimics the natural progression of DNA synthesis.[50,102,103] Our assay employs DNA templates, either containing or lacking the G4 sequence, annealed to a fluorescently labeled primer, along with a DNA polymerase, dNTPs, and essential cofactors like Mg^{2+} (Fig. 5A and D). As synthesis proceeds, the extension of the labeled primer is observed; when the polymerase encounters a blockage, it pauses and ultimately dissociates, resulting in truncated products compared to full-length extensions.[50,102,103] These products are then separated *via* denaturing polyacrylamide gel electrophoresis (PAGE) and visualized.

In the absence of **DBI-POE**, the polymerase efficiently synthesized full-length products without interruption (Fig. 5B and C). However, when **DBI-POE** was added in the dark, a prominent pause site emerged at T20, immediately upstream of the first guanine tract, consistent with the structural stabilization observed *via* CD spectroscopy (Fig. 4C) and previously reported for other G4 ligands (Fig. 5B and C).[27,50,102] Under light irradiation, additional pausing occurred at positions T11 and G10, and after 20 minutes, polymerase processivity was almost completely halted (Fig. 5B and C). We speculate that **DBI-POE** localizes near G9 and G10 within the *c-MYC* G4 structure, thereby triggering its oxidation.

To further explore the binding site of **DBI-POE** in *c-MYC* Pu22, we conducted molecular docking and MD simulations

and investigated the intercalation of **DBI-POE** by opening the 3′-end and central tetrads, where G10 and G9 are located, through a combination of MD and umbrella sampling techniques (see ESI† for details). After equilibrating the final opened G4 structure, docking calculations identified the most populated intercalated poses. As illustrated in Fig. S26 (ESI†), we distinguish two main binding sites depending on the moiety of **DBI-POE** that stacks between the tetrads: the hydrophobic core (pose A) or the hydrophilic arm (pose B). The MD simulations (Fig. S28, ESI†) showed that pose B is not stable, as it disrupted the tetrad integrity in the G4 (Fig. S28B, ESI†), whereas pose A remained stable (Fig. 4D and Fig. S28A, ESI†). This indicates that pose A is the most probable **DBI-POE** binding site as, in accordance with experimental studies, it stabilizes the G4 in the dark.

The overall reduction in *TET* label fluorescence is attributable to light-induced bleaching. To test our hypothesis that these lesions resulted from guanine oxidation, we designed a *c-MYC* Pu22 template with site-specific 8-oxoG substitutions at positions G10 and G9, which are predicted to be the primary oxidation targets (Fig. 5A). This modified template produced a pausing pattern nearly identical to that observed with light-activated **DBI-POE**, although with a more intense signal due to the absence of light-mediated *TET* bleaching, ultimately leading to complete polymerase arrest at the corresponding sites (Fig. 5B). This conclusively demonstrates that **DBI-POE** induces site-specific oxidative damage *via* the formation of 8-oxoG.

As control, we used a DNA template lacking any G4 motif (Fig. 5D).[102] Under both dark and light conditions, no polymerase pausing was observed (Fig. 5E and F). Similarly to the G4 reaction, light-mediated bleaching of *TET* label caused an overall decrease of the signal (Fig. 5E and F). These results indicate that **DBI-POE**'s $^1O_2$-induced damage is selective for G4 structures and does not cause nonspecific DNA damage when **DBI-POE** remains in its unbound state.

We further evaluated the structural impact of 8-oxoG incorporation on the *c-MYC* Pu22 G4 scaffold using MD simulations. While formation of a single 8-oxoG at G10 preserved the overall G4 conformation, simultaneous substitution at G10 and G9 resulted in significant structural disruption (Fig. 6). These computational insights suggest that multiple oxidative lesions are required to compromise G4 stability and underscore the importance of precise PS positioning for effective phototherapeutic activity.

Collectively, these integrated studies reveal a novel, light-mediated mechanism in which **DBI-POE** precisely oxidizes and disrupts G4 structures. This strategy holds significant promise for targeted PDT, as G4-targeted PSs can downregulate cancer-associated genes by destabilizing their regulatory G4 elements.[62]

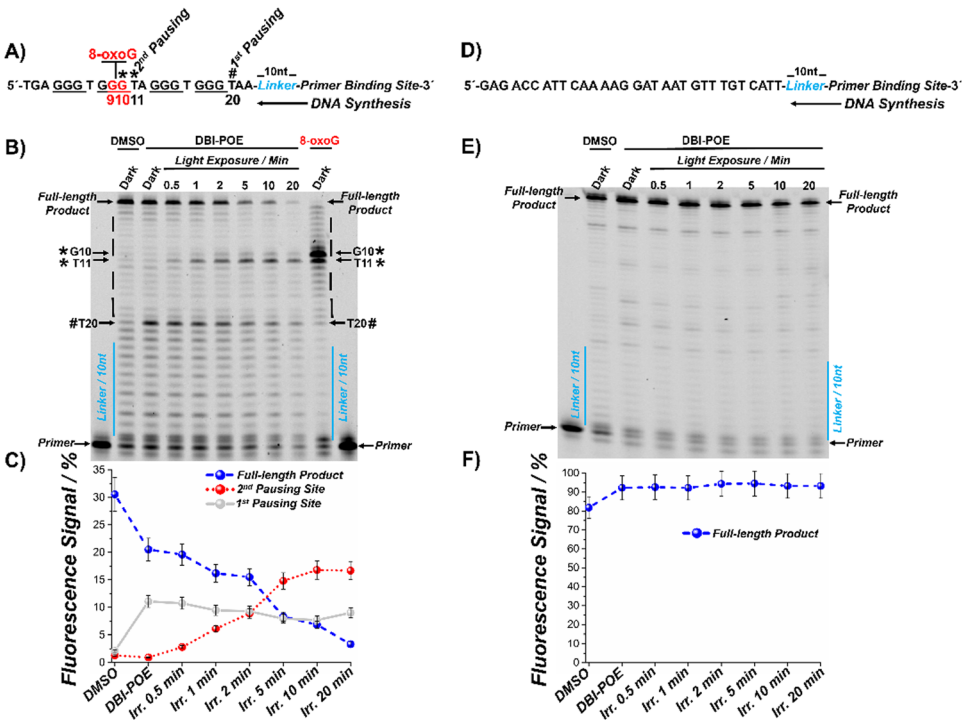

Fig. 5 Oxidative DNA photodamage mediated by **DBI-POE** revealed by primer extension assays at single-base pair resolution. (A) Sequence of the *c-MYC* Pu22 template used in the assay. Guanine residues involved in G4 formation are underlined. Hash marks and asterisks denote the first and second pausing sites, respectively, detected in panel (B), and chemically inserted 8-oxoG modifications are highlighted in red. (B) Representative primer extension assay using the *c-MYC* Pu22 template. (C) Relative quantification of full-length products, 1st and 2nd pausing sites from panel (B). (D) Sequence of the non-G4 DNA template used as a control. (E) Primer extension assay with the non-G4 template. (F) Relative quantification of full-length products from panel (E). All experiments were performed using **DBI-POE** = 1 μM. Black arrows indicate the start of the reaction (non-extended primer), as well as the pausing sites and full-length products. (B and E) Irradiation was carried out at 460–495 nm over various time intervals.

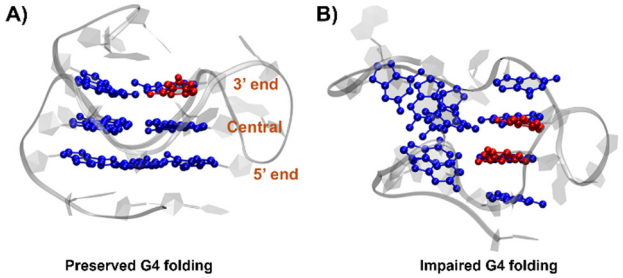

Fig. 6 Representative MD structures of oxidized *c-MYC* Pu22 with a single mutation at G10 (A), and two mutations at G10 and G9 (B) from the dbscan clustering of the last 1 μs of the MD production. The 8-oxoG mutations are indicated in red.

Conclusions

G4 structures are significantly overrepresented in cancer cells, making them appealing targets for precision therapy.[33,104,105] Their enrichment in the promoter regions of difficult-to-treat oncogenes,[46] such as *MYC* and *HIF*, suggests that small molecule ligands that stabilize G4s can effectively hinder DNA and/or RNA polymerase progression, thereby triggering replication stress, DNA damage, and ultimately cell death.[48,74,77,78]

Despite significant progress in developing light-activated compounds that modulate G4 activity with high spatiotemporal control, several challenges persist.[106–108] In particular, the limited bidirectional modulation of molecular photochromes calls for more versatile photoregulation strategies.[51,108–110] Moreover, while the susceptibility of G4s to oxidation presents an opportunity, it also poses a challenge, especially since current G4-targeting PSs predominantly rely on highly reactive and poorly selective type I mechanisms that have not adequately addressed this vulnerability.[59–63] To overcome these limitations, we introduce **DBI-POE**, a novel PS that transitions from a type I to a type II mechanism upon binding to G4 structures, thereby combining both structure-specific and site-specific oxidative damage.

Our comprehensive studies revealed that **DBI-POE** binds selectively to parallel and hybrid G4 conformations, triggering supramolecular disassembly that "turns on" its fluorescence and significantly enhances two-photon absorption in the NIR region. Photophysical analyses showed that while free **DBI-POE** predominantly generates ROS *via* a type I pathway (producing $O_2^{\bullet-}$ and $OH^{\bullet}$ species), its complexation with G4s reprograms its photochemistry toward a highly selective type II mechanism that yields $^1O_2$. This switching mechanism was rigorously supported by multiple discriminant assays. In-depth biophysical studies confirm that light-activated **DBI-POE** induces selective oxidative damage and unfolding of the G4 scaffold.

Further validation came from primer extension assays, which demonstrated site-specific stalling at oxidatively modified guanine residues, as well as from MD simulations that highlighted structural destabilization associated with 8-oxoG formation. Importantly, the oxidative damage induced by **DBI-POE** was confined to the DNA template containing the G4 structure, leaving the non-G4 template unaffected, underscoring its exceptional selectivity.

Collectively, these findings provide unprecedented mechanistic insights into a G4-targeted PS and highlight the potential of **DBI-POE** as a platform for developing next-generation agents for precision photodynamic anticancer therapy.

Ongoing studies are actively investigating its photoactivation in cells, both as a standalone approach and in combination with delivery systems such as G4 aptamers. These strategies are also being evaluated alongside DNA-damaging agents and/or DNA damage response (DDR) inhibitors, with the aim of further enhancing the overall phototherapeutic efficacy.

Author contributions

Conceptualization (M. Deiana and C. Cabanetos), synthesis and characterization of the compound (D. Puchán Sánchez, A. Kassem), photophysical, biophysical and biochemical studies (K. Saczuk, M. V. Cottini, M. Dudek, L. M. Mazur, C. Monnereau, J. Jamroskovic, M. Deiana), supervision (J. J. Nogueira, L. Martínez-Fernández, J. Jamroskovic, C. Cabanetos, M. Deiana), computational data (L. López-Pacios, J. J. Nogueira, L. Martínez-Fernández), writing original draft (M. Deiana with inputs from all authors), funding acquisition (J. J. Nogueira, L. Martínez-Fernández, J. Jamroskovic, C. Cabanetos, M. Deiana), project administration (M. Deiana), revision of the manuscript (M. Deiana and K. Saczuk). All authors approved the final version of the manuscript.

Data availability

All the data that support this study are included in this article and its ESI.†

Conflicts of interest

There are no conflicts to declare.

Acknowledgements

M. Deiana would like to acknowledge financial support from project no. 2022/47/P/NZ5/01156, which is co-funded by the National Science Centre and the European Union's Horizon 2020 research and innovation program under the Marie Skłodowska-Curie grant agreement no. 945339. Funding for J. Jamroskovic was provided by the IMPULZ program of the Slovak Academy of Sciences under the Agreement on the Provision of Funds No. IM-2022-62. L. López-Pacios acknowledges the FPU22/02196 grant from the Spanish Ministry of Science, Innovation and Universities (MICINN). L. Martínez-Fernández acknowledges the grant PID2023-151719NA-I00 funded by MICIU/AEI/10.13039/501100011033 and FEDER, UE. J. Nogueira thanks the Spanish Ministry of Science and Innovation for funding support through the project CNS2022-135720 (MCIN/AEI/10.13039/501100011033). This research project was made possible through the access granted by the Galician Supercomputing Center (CESGA) to its supercomputing infrastructure. The authors thank

Dr Aeson Chang at Monash University (Australia) for carefully reading the manuscript and providing insightful comments. We acknowledge Protein Production Sweden (PPS) for providing facilities and experimental support. PPS is funded by the Swedish Research Council as a national research infrastructure. We thank the members of Dr. Barak's laboratory (Slovak Academy of Sciences) for their help with the initial biochemical experiments. We also thank Dr. Barancik (Slovak Academy of Sciences) for providing access to the Typhoon scanner.

Notes and references

1 P. Kobauri, F. J. Dekker, W. Szymanski and B. L. Feringa, *Angew. Chem., Int. Ed.*, 2023, **62**, e202300681.
2 X. Li, J. F. Lovell, J. Yoon and X. Chen, *Nat. Rev. Clin. Oncol.*, 2020, **17**, 657–674.
3 B. M. Vickerman, E. M. Zywot, T. K. Tarrant and D. S. Lawrence, *Nat. Rev. Chem.*, 2021, **5**, 816–834.
4 W. A. Velema, W. Szymanski and B. L. Feringa, *J. Am. Chem. Soc.*, 2014, **136**, 2178–2191.
5 T. C. Pham, V.-N. Nguyen, Y. Choi, S. Lee and J. Yoon, *Chem. Rev.*, 2021, **121**, 13454–13619.
6 X. Zhao, J. Liu, J. Fan, H. Chao and X. Peng, *Chem. Soc. Rev.*, 2021, **50**, 4185–4219.
7 V.-N. Nguyen, Y. Yan, J. Zhao and J. Yoon, *Acc. Chem. Res.*, 2021, **54**, 207–220.
8 B. Lu, L. Wang, H. Tang and D. Cao, *J. Mater. Chem. B*, 2023, **11**, 4600–4618.
9 G. Xu, C. Li, C. Chi, L. Wu, Y. Sun, J. Zhao, X.-H. Xia and S. Gou, *Nat. Commun.*, 2022, **13**, 3064.
10 K.-X. Teng, L.-Y. Niu, N. Xie and Q.-Z. Yang, *Nat. Commun.*, 2022, **13**, 6179.
11 Y. Tang, Y. Li, B. Li, W. Song, G. Qi, J. Tian, W. Huang, Q. Fan and B. Liu, *Nat. Commun.*, 2024, **15**, 2530.
12 Z. Li, Z. Zhang, L. Ma, H. Wen, M. Kang, D. Li, W. Zhang, S. Luo, W. Wang, M. Zhang, D. Wang, H. Li, X. Li and H. Wang, *Angew. Chem., Int. Ed.*, 2024, **63**, e202400049.
13 K.-X. Teng, L.-Y. Niu and Q.-Z. Yang, *J. Am. Chem. Soc.*, 2023, **145**, 4081–4087.
14 J. Zhuang, B. Wang, H. Chen, K. Zhang, N. Li, N. Zhao and B. Z. Tang, *ACS Nano*, 2023, **17**, 9110–9125.
15 Y. Wang, S. Xu, L. Shi, C. Teh, G. Qi and B. Liu, *Angew. Chem., Int. Ed.*, 2021, **60**, 14945–14953.
16 M. Wu, X. Liu, H. Chen, Y. Duan, J. Liu, Y. Pan and B. Liu, *Angew. Chem., Int. Ed.*, 2021, **60**, 9093–9098.
17 H. Wang, Q. Li, P. Alam, H. Bai, V. Bhalla, M. R. Bryce, M. Cao, C. Chen, S. Chen, X. Chen, Y. Chen, Z. Chen, D. Dang, D. Ding, S. Ding, Y. Duo, M. Gao, W. He, X. He, X. Hong, Y. Hong, J.-J. Hu, R. Hu, X. Huang, T. D. James, X. Jiang, G.-I. Konishi, R. T. K. Kwok, J. W. Y. Lam, C. Li, H. Li, K. Li, N. Li, W.-J. Li, Y. Li, X.-J. Liang, Y. Liang, B. Liu, G. Liu, X. Liu, X. Lou, X.-Y. Lou, L. Luo, P. R. McGonigal, Z.-W. Mao, G. Niu, T. C. Owyong, A. Pucci, J. Qian, A. Qin, Z. Qiu, A. L. Rogach, B. Situ, K. Tanaka, Y. Tang, B. Wang, D. Wang, J. Wang, W. Wang, W.-X. Wang, W.-J. Wang, X. Wang, Y.-F. Wang, S. Wu, Y. Wu, Y. Xiong, R. Xu, C. Yan, S. Yan, H.-B. Yang, L.-L. Yang, M. Yang, Y.-W. Yang, J. Yoon, S.-Q. Zang, J. Zhang, P. Zhang, T. Zhang, X. Zhang, N. Zhao, Z. Zhao, J. Zheng, L. Zheng, Z. Zheng, M.-Q. Zhu, W.-H. Zhu, H. Zou and B. Z. Tang, *ACS Nano*, 2023, **17**, 14347–14405.
18 N. Kwon, H. Weng, M. A. Rajora and G. Zheng, *Angew. Chem., Int. Ed.*, 2025, e202423348.
19 L. Zhang, F. Chai, H. Dong, Y. Bao, K. Yan, S. Min, Y. Yao, S. Li, Y. Liu, T. Gao, J. Wang and Y. Liu, *J. Phys. Chem. Lett.*, 2024, **15**, 10866–10872.
20 G. Liu, H. Wang, C. Shi, G. Chen, Y. Wang, W. Huang and H. Zhao, *Chem. Commun.*, 2022, **58**, 10813–10816.
21 J. Mei, N. L. C. Leung, R. T. K. Kwok, J. W. Y. Lam and B. Z. Tang, *Chem. Rev.*, 2015, **115**, 11718–11940.
22 F. Bouhedda, K. T. Fam, M. Collot, A. Autour, S. Marzi, A. Klymchenko and M. Ryckelynck, *Nat. Chem. Biol.*, 2020, **16**, 69–76.
23 I. O. Aparin, R. Yan, R. Pelletier, A. A. Choi, D. I. Danylchuk, K. Xu and A. S. Klymchenko, *J. Am. Chem. Soc.*, 2022, **144**, 18043–18053.
24 M. Collot, P. Ashokkumar, H. Anton, E. Boutant, O. Faklaris, T. Galli, Y. Mély, L. Danglot and A. S. Klymchenko, *Cell Chem. Biol.*, 2019, **26**, 600–614.e607.
25 K. Saczuk, M. Dudek, K. Matczyszyn and M. Deiana, *Nanoscale Horiz.*, 2024, **9**, 1390–1416.
26 M. Deiana, K. Chand, J. Jamroskovic, I. Obi, E. Chorell and N. Sabouri, *Angew. Chem., Int. Ed.*, 2020, **59**, 896–902.
27 M. Deiana, K. Chand, J. Jamroskovic, R. N. Das, I. Obi, E. Chorell and N. Sabouri, *Nanoscale*, 2020, **12**, 12950–12957.
28 V. Grande, C.-A. Shen, M. Deiana, M. Dudek, J. Olesiak-Banska, K. Matczyszyn and F. Würthner, *Chem. Sci.*, 2018, **9**, 8375–8381.
29 M. Deiana, K. Chand, E. Chorell and N. Sabouri, *J. Phys. Chem. Lett.*, 2023, **14**, 1862–1869.
30 V. Grande, F. Doria, M. Freccero and F. Würthner, *Angew. Chem., Int. Ed.*, 2017, **56**, 7520–7524.
31 M. Zuffo, A. Guédin, E.-D. Leriche, F. Doria, V. Pirota, V. Gabelica, J.-L. Mergny and M. Freccero, *Nucleic Acids Res.*, 2018, **46**, e115.
32 A. Pandith, Y. Luo, Y. Jang, J. Bae and Y. Kim, *Angew. Chem., Int. Ed.*, 2023, **62**, e202215049.
33 G. Biffi, D. Tannahill, J. McCafferty and S. Balasubramanian, *Nat. Chem.*, 2013, **5**, 182–186.
34 G. Biffi, M. Di Antonio, D. Tannahill and S. Balasubramanian, *Nat. Chem.*, 2014, **6**, 75–80.
35 P. A. Summers, B. W. Lewis, J. Gonzalez-Garcia, R. M. Porreca, A. H. M. Lim, P. Cadinu, N. Martin-Pintado, D. J. Mann, J. B. Edel, J. B. Vannier, M. K. Kuimova and R. Vilar, *Nat. Commun.*, 2021, **12**, 162.
36 M. Di Antonio, A. Ponjavic, A. Radzevičius, R. T. Ranasinghe, M. Catalano, X. Zhang, J. Shen, L.-M. Needham, S. F. Lee, D. Klenerman and S. Balasubramanian, *Nat. Chem.*, 2020, **12**, 832–837.
37 K. T. McQuaid, A. Pipier, C. J. Cardin and D. Monchaud, *Nucleic Acids Res.*, 2022, **50**, 12636–12656.
38 J. L. Huppert and S. Balasubramanian, *Nucleic Acids Res.*, 2005, **33**, 2908–2916.

39 V. S. Chambers, G. Marsico, J. M. Boutell, M. Di Antonio, G. P. Smith and S. Balasubramanian, *Nat. Biotechnol.*, 2015, **33**, 877–881.
40 R. Hänsel-Hertsch, D. Beraldi, S. V. Lensing, G. Marsico, K. Zyner, A. Parry, M. Di Antonio, J. Pike, H. Kimura, M. Narita, D. Tannahill and S. Balasubramanian, *Nat. Genet.*, 2016, **48**, 1267–1272.
41 D. Varshney, J. Spiegel, K. Zyner, D. Tannahill and S. Balasubramanian, *Nat. Rev. Mol. Cell Biol.*, 2020, **21**, 459–474.
42 N. Kosiol, S. Juranek, P. Brossart, A. Heine and K. Paeschke, *Mol. Cancer*, 2021, **20**, 40.
43 M. Sauer and K. Paeschke, *Biochem. Soc. Trans.*, 2017, **45**, 1173–1182.
44 Kevin K.-P. Yan, I. Obi and N. Sabouri, *Nucleic Acids Res.*, 2021, **49**, 8339–8354.
45 P. Lejault, J. Mitteaux, F. R. Sperti and D. Monchaud, *Cell Chem. Biol.*, 2021, **28**, 436–455.
46 S. Neidle, *Nat. Rev. Chem.*, 2017, **1**, 0041.
47 S. Neidle, *J. Med. Chem.*, 2016, **59**, 5987–6011.
48 D. R. Calabrese, X. Chen, E. C. Leon, S. M. Gaikwad, Z. Phyo, W. M. Hewitt, S. Alden, T. A. Hilimire, F. He, A. M. Michalowski, J. K. Simmons, L. B. Saunders, S. Zhang, D. Connors, K. J. Walters, B. A. Mock and J. S. Schneekloth, *Nat. Commun.*, 2018, **9**, 4229.
49 H. Xu, M. Di Antonio, S. McKinney, V. Mathew, B. Ho, N. J. O'Neil, N. D. Santos, J. Silvester, V. Wei, J. Garcia, F. Kabeer, D. Lai, P. Soriano, J. Banáth, D. S. Chiu, D. Yap, D. D. Le, F. B. Ye, A. Zhang, K. Thu, J. Soong, S.-C. Lin, A. H. C. Tsai, T. Osako, T. Algara, D. N. Saunders, J. Wong, J. Xian, M. B. Bally, J. D. Brenton, G. W. Brown, S. P. Shah, D. Cescon, T. W. Mak, C. Caldas, P. C. Stirling, P. Hieter, S. Balasubramanian and S. Aparicio, *Nat. Commun.*, 2017, **8**, 14432.
50 J. Jamroskovic, M. Doimo, K. Chand, I. Obi, R. Kumar, K. Brännström, M. Hedenström, R. Nath Das, A. Akhunzianov, M. Deiana, K. Kasho, S. Sulis Sato, P. L. Pourbozorgi, J. E. Mason, P. Medini, D. Öhlund, S. Wanrooij, E. Chorell and N. Sabouri, *J. Am. Chem. Soc.*, 2020, **142**, 2876–2888.
51 M. Dudek, L. López-Pacios, N. Sabouri, J. J. Nogueira, L. Martinez-Fernandez and M. Deiana, *Angew. Chem., Int. Ed.*, 2025, **64**, e202413000.
52 M. Deiana, I. Obi, M. Andreasson, S. Tamilselvi, K. Chand, E. Chorell and N. Sabouri, *ACS Chem. Biol.*, 2021, **16**, 1365–1376.
53 A. M. Fleming and C. J. Burrows, *J. Am. Chem. Soc.*, 2020, **142**, 1115–1136.
54 A. M. Fleming, B. L. Guerra Castañaza Jenkins, B. A. Buck and C. J. Burrows, *J. Am. Chem. Soc.*, 2024, **146**, 11364–11370.
55 A. M. Fleming and C. J. Burrows, *NAR Cancer*, 2021, **3**, zcab038.
56 Y. Ding, A. M. Fleming and C. J. Burrows, *J. Am. Chem. Soc.*, 2017, **139**, 2569–2572.
57 P. Di Mascio, G. R. Martinez, S. Miyamoto, G. E. Ronsein, M. H. G. Medeiros and J. Cadet, *Chem. Rev.*, 2019, **119**, 2043–2086.
58 J. Cadet, K. J. A. Davies, M. H. G. Medeiros, P. Di Mascio and J. R. Wagner, *Free Radicals Biol. Med.*, 2017, **107**, 13–34.
59 W. Chen, Y. Zhang, H.-B. Yi, F. Wang, X. Chu and J.-H. Jiang, *Angew. Chem., Int. Ed.*, 2023, **62**, e202300162.
60 X. Zhang, J. Wang and M.-H. Hu, *ACS Pharmacol. Transl. Sci.*, 2024, **7**, 2174–2184.
61 X. Zhang and M.-H. Hu, *Sens. Actuators, B*, 2025, **425**, 136952.
62 K. Kawauchi, W. Sugimoto, T. Yasui, K. Murata, K. Itoh, K. Takagi, T. Tsuruoka, K. Akamatsu, H. Tateishi-Karimata, N. Sugimoto and D. Miyoshi, *Nat. Commun.*, 2018, **9**, 2271.
63 L. Holden, R. C. Curley, G. Avella, C. Long and T. E. Keyes, *Angew. Chem., Int. Ed.*, 2024, **63**, e202408581.
64 M. Bartlett, J. Burke, P. Sherin, M. K. Kuimova, M. Barahona and R. Vilar, *Chem. – Eur. J.*, 2024, **30**, e202402465.
65 B. Halliwell, A. Adhikary, M. Dingfelder and M. Dizdaroglu, *Chem. Soc. Rev.*, 2021, **50**, 8355–8360.
66 M. Deiana, P. Josse, C. Dalinot, A. Osmolovskyi, P. S. Marqués, J. M. A. Castán, L. Abad Galán, M. Allain, L. Khrouz, O. Maury, T. Le Bahers, P. Blanchard, S. Dabos-Seignon, C. Monnereau, N. Sabouri and C. Cabanetos, *Commun. Chem.*, 2022, **5**, 142.
67 M. Deiana, J. M. Andrés Castán, P. Josse, A. Kahsay, D. P. Sánchez, K. Morice, N. Gillet, R. Ravindranath, A. K. Patel, P. Sengupta, I. Obi, E. Rodriguez-Marquez, L. Khrouz, E. Dumont, L. Abad Galán, M. Allain, B. Walker, H. S. Ahn, O. Maury, P. Blanchard, T. Le Bahers, D. Öhlund, J. von Hofsten, C. Monnereau, C. Cabanetos and N. Sabouri, *Nucleic Acids Res.*, 2023, **51**, 6264–6285.
68 D. P. Sánchez, K. Morice, M. G. Mutovska, L. Khrouz, P. Josse, M. Allain, F. Gohier, P. Blanchard, C. Monnereau, T. Le Bahers, N. Sabouri, Y. Zagranyarski, C. Cabanetos and M. Deiana, *J. Mater. Chem. B*, 2024, **12**, 8107–8121.
69 A. Merabti, D. P. Sánchez, A. Nocentini, L. M. A. Ali, C. Nguyen, D. Durand, K. Hamon, T. Ghanem, P. Arnoux, P. Josse, C. Frochot, R. Zalubovskis, S. Richeter, M. Gary-Bobo, C. T. Supuran, C. Cabanetos, J.-Y. Winum and S. Clément, *Mater. Adv.*, 2024, **5**, 4172–4177.
70 A. Nsubuga, K. Morice, N. Fayad, F. Pini, V. Josserand, X. Le Guével, A. Alhabi, M. Henry, D. Puchán Sánchez, N. Plassais, P. Josse, J. Boixel, P. Blanchard, C. Cabanetos and N. Hildebrandt, *Adv. Funct. Mater.*, 2024, 2410077.
71 K. Saczuk, A. Kassem, M. Dudek, D. P. Sánchez, L. Khrouz, M. Allain, G. C. Welch, N. Sabouri, C. Monnereau, P. Josse, C. Cabanetos and M. Deiana, *J. Phys. Chem. Lett.*, 2025, **16**, 2273–2282.
72 E. Rodriguez-Marquez, H. Nord, D. Puchán Sánchez, A. Kassem, J. M. Andrés Castán, M. Deiana, C. Cabanetos, N. Sabouri and J. von Hofsten, *ACS Pharmacol. Transl. Sci.*, 2025, DOI: **10.1021/acsptsci.5c00061**.
73 V. Grande, B. Soberats, S. Herbst, V. Stepanenko and F. Würthner, *Chem. Sci.*, 2018, **9**, 6904–6911.
74 A. Berner, R. N. Das, N. Bhuma, J. Golebiewska, A. Abrahamsson, M. Andréasson, N. Chaudhari, M. Doimo, P. P. Bose, K. Chand, R. Strömberg, S. Wanrooij and E. Chorell, *J. Am. Chem. Soc.*, 2024, **146**, 6926–6935.

75 P. Thordarson, *Chem. Soc. Rev.*, 2011, **40**, 1305–1323.
76 B.-C. Zhu, J. He, X.-Y. Xia, J. Jiang, W. Liu, L.-Y. Liu, B.-B. Liang, H.-G. Yao, Z. Ke, W. Xia and Z.-W. Mao, *Chem. Sci.*, 2022, **13**, 8371–8379.
77 S. J. Welsh, A. G. Dale, C. M. Lombardo, H. Valentine, M. de la Fuente, A. Schatzlein and S. Neidle, *Sci. Rep.*, 2013, **3**, 2799.
78 H. Chen, H. Long, X. Cui, J. Zhou, M. Xu and G. Yuan, *J. Am. Chem. Soc.*, 2014, **136**, 2583–2591.
79 P. Agrawal, E. Hatzakis, K. Guo, M. Carver and D. Yang, *Nucleic Acids Res.*, 2013, **41**, 10584–10592.
80 I. Obi, M. Rentoft, V. Singh, J. Jamroskovic, K. Chand, E. Chorell, F. Westerlund and N. Sabouri, *Nucleic Acids Res.*, 2020, **48**, 10998–11015.
81 M. Deiana, J. Jamroskovic, I. Obi and N. Sabouri, *Chem. Commun.*, 2020, **56**, 14251–14254.
82 A. Ghosh, M. Trajkovski, M.-P. Teulade-Fichou, V. Gabelica and J. Plavec, *Angew. Chem., Int. Ed.*, 2022, **61**, e202207384.
83 B. Prasad, M. Doimo, M. Andréasson, V. L'Hôte, E. Chorell and S. Wanrooij, *Chem. Sci.*, 2022, **13**, 2347–2354.
84 A. Soleimany, D. K. Aghmiouni, M. Amirikhah, M. A. Shokrgozar, S. Khoee and B. Sarmento, *Adv. Funct. Mater.*, 2024, 2408594.
85 M. Deiana, B. Mettra, L. Martinez-Fernandez, L. M. Mazur, K. Pawlik, C. Andraud, M. Samoc, R. Improta, C. Monnereau and K. Matczyszyn, *J. Phys. Chem. Lett.*, 2017, **8**, 5915–5920.
86 S. Liu, L. Bu, Y. Zhang, J. Yan, L. Li, G. Li, Z. Song and J. Huang, *Anal. Chem.*, 2021, **93**, 5267–5276.
87 T.-C. Lin, W. Chien, L. M. Mazur, Y.-Y. Liu, K. Jakubowski, K. Matczyszyn, M. Samoc and R. W. Amini, *J. Mater. Chem. C*, 2017, **5**, 8219–8232.
88 L. M. Mazur, T. Roland, S. Leroy-Lhez, V. Sol, M. Samoc, I. D. W. Samuel and K. Matczyszyn, *J. Phys. Chem. B*, 2019, **123**, 4271–4277.
89 T. Entradas, S. Waldron and M. Volk, *J. Photochem. Photobiol., B*, 2020, **204**, 111787.
90 Y.-L. Zeng, L.-Y. Liu, T.-Z. Ma, Y. Liu, B. Liu, W. Liu, Q.-H. Shen, C. Wu and Z.-W. Mao, *Angew. Chem., Int. Ed.*, 2024, **63**, e202410803.
91 F. J. Ballester, E. Ortega, D. Bautista, M. D. Santana and J. Ruiz, *Chem. Commun.*, 2020, **56**, 10301–10304.
92 J. Bonelli, E. Ortega-Forte, G. Vigueras, J. Follana-Berná, P. Ashoo, D. Abad-Montero, N. Isidro, M. López-Corrales, A. Hernández, J. Ortiz, E. Izquierdo-García, M. Bosch, J. Rocas, Á. Sastre-Santos, J. Ruiz and V. Marchán, *ACS Appl. Mater. Interfaces*, 2024, **16**, 38916–38930.
93 M. Bregnhøj, F. Thorning and P. R. Ogilby, *Chem. Rev.*, 2024, **124**, 9949–10051.
94 J. Zhuang, S. Liu, B. Li, Z. Li, C. Wu, D. Xu, W. Pan, Z. Li, X. Liu and B. Liu, *Angew. Chem., Int. Ed.*, 2024, e202420643.
95 R. del Villar-Guerra, J. O. Trent and J. B. Chaires, *Angew. Chem., Int. Ed.*, 2018, **57**, 7171–7175.
96 B. G. Kim, H. M. Evans, D. N. Dubins and T. V. Chalikian, *Biochemistry*, 2015, **54**, 3420–3430.
97 L. De Paepe, A. Madder and E. Cadoni, *Small Methods*, 2024, **8**, 2301570.
98 S. Bielskutė, J. Plavec and P. Podbevšek, *J. Am. Chem. Soc.*, 2019, **141**, 2594–2603.
99 S. Bielskutė, J. Plavec and P. Podbevšek, *Nucleic Acids Res.*, 2021, **49**, 2346–2356.
100 A. M. Fleming, J. Zhou, S. S. Wallace and C. J. Burrows, *ACS Cent. Sci.*, 2015, **1**, 226–233.
101 S. A. Johnson, T. Paul, S. L. Sanford, B. L. Schnable, A. C. Detwiler, S. A. Thosar, B. Van Houten, S. Myong and P. L. Opresko, *Nucleic Acids Res.*, 2024, **52**, 1763–1778.
102 J. Jamroskovic, M. Deiana and N. Sabouri, *Biochimie*, 2022, **199**, 81–91.
103 M. Deiana, M. Mosser, T. Le Bahers, E. Dumont, M. Dudek, S. Denis-Quanquin, N. Sabouri, C. Andraud, K. Matczyszyn, C. Monnereau and L. Guy, *Nanoscale*, 2021, **13**, 13795–13808.
104 G. Biffi, D. Tannahill, J. Miller, W. J. Howat and S. Balasubramanian, *PLoS One*, 2014, **9**, e102711.
105 R. Hänsel-Hertsch, A. Simeone, A. Shea, W. W. I. Hui, K. G. Zyner, G. Marsico, O. M. Rueda, A. Bruna, A. Martin, X. Zhang, S. Adhikari, D. Tannahill, C. Caldas and S. Balasubramanian, *Nat. Genet.*, 2020, **52**, 878–883.
106 M. P. O'Hagan, J. Ramos-Soriano, S. Haldar, S. Sheikh, J. C. Morales, A. J. Mulholland and M. C. Galan, *Chem. Commun.*, 2020, **56**, 5186–5189.
107 J. Ramos-Soriano and M. C. Galan, *JACS Au*, 2021, **1**, 1516–1526.
108 M. P. O'Hagan, S. Haldar, M. Duchi, T. A. A. Oliver, A. J. Mulholland, J. C. Morales and M. C. Galan, *Angew. Chem., Int. Ed.*, 2019, **58**, 4334–4338.
109 M. Dudek, L. López-Pacios, N. Sabouri, J. J. Nogueira, L. Martinez-Fernandez and M. Deiana, *J. Phys. Chem. Lett.*, 2024, **15**, 9757–9765.
110 A. Matusiak, M. Drąg, M. Deiana, M. J. Janicki and M. Dudek, *Chem. – Eur. J.*, 2025, e202404365.